Chapter 28
Nanoscale Sampling of Optical Signals: Application to High-Resolution Spectroscopy

Guillermo Martin, Alain Morand, Myriam Bonduelle, Ciro D'Amico, Razvan Stoian, Javier Rodriguez Vazquez de Aldana, and Carolina Romero Vazquez

Abstract Direct laser writing is a powerful technique for the development of photonic devices, namely, by allowing 3D structuring and generation of waveguides and other optical functions in bulk dielectrics by locally changing the material refractive index. One of the main interests of the 3D design is the possibility to avoid in-plane crossings of waveguides that can induce losses and crosstalk in future multi-telescope beam combiners. Another powerful advantage of the direct laser writing technique is the ability to directly photo-write nanoscale dielectric discontinuities, allowing to extract light from a waveguide in a controlled way. This allows to periodically sample an optical signal confined in a waveguide and obtain, by dedicated Fourier transform algorithms, the high-resolution spectrum of the optical source while maintaining a very robust, compact optical device. The versatility of laser writing allows to adapt the technique to different transparency range materials (visible, near-, or mid-infrared) and designs and therefore to address a variety of spectral windows and optical functions with a single technological tool. Finally, direct laser writing allows rapid fabrication of complex optical

G. Martin (✉)
Université Grenoble Alpes, CNRS, IPAG, Grenoble, France
e-mail: guillermo.martin@univ-grenoble-alpes.fr

A. Morand
Université Grenoble Alpes, CNRS, Grenoble INP, IMEP-LAHC, Grenoble, France

M. Bonduelle
Université Grenoble Alpes, CNRS, IPAG, Grenoble, France

C. D'Amico · R. Stoian
Laboratoire Hubert Curien, UMR 5516 CNRS, Université de Lyon, Université Jean Monnet, St. Etienne, France

J. Rodriguez Vazquez de Aldana · C. Romero Vazquez
Grupo de Investigacion en Aplicaciones del Laser y Fotonica, Facultad de Ciencias, Universidad de Salamanca, Salamanca, Spain

chips (photonic functions, material ablation, electrode patterning), without needing multiple lithographic steps.

In this chapter, different techniques will be described for waveguide and nano-scattering center fabrication, and it will be shown how this can be used in integrated optics spectroscopy. After describing the principle of the Fourier transform-integrated optics spectrometer, we will explain how laser writing can address the strong requirements needed to achieve high-resolution, high spectral range spectroscopy. In particular, it will be demonstrated that using laser writing to fabricate 3D nano-antennas, the directivity of the sampled signal can be improved. The development of these techniques in electro-optic crystals is also interesting in order to increase the signal-to-noise ratio and the detected spectral window. In a final paragraph, the use of 3D laser writing of waveguides to achieve pupil remapping will be shown, together with some direct applications: image reconstruction, spectro-imaging, and wavelength filtering.

Keywords Direct laser-written waveguides · Nano-scattering centers · 3D beam combiners · Electro-optic modulation · Stationary wave Fourier transform spectrometry: SWIFTS · Temporal/spatial multiplexing · Arrayed waveguide structures · Spectro-interferometers · Pupil remapping

1 DLW for Waveguide Fabrication

As discussed in the previous chapters, the fundamental result of direct laser writing (DLW) is the possibility to modify the refractive index of the material under exposure [11]. The technique consists in focusing the laser beam into the glass [45], crystal [24], or polymer [58], usually by using high numerical aperture (NA) microscope objectives.

The material is modified in the focal region, where the intensity reached by the focused beam is sufficiently high that strong-field nonlinear ionization processes (multiphoton, tunnel, avalanche) are induced. The locally absorbed laser energy induces a local elevation of the temperature in the material, and eventually thermo-dynamic and hydrodynamic phenomena of matter modification and rearrangement can happen (phase transitions, material expansion and cavitation, cooling). The permanent change is represented by a local modification of the refractive index, which can be either positive, corresponding to a local smooth densification (the so-called type I refractive index change), or negative, corresponding to a local rarefaction (the so-called type II index change). In the case of smooth type I refractive index changes, straight or curved waveguides can be realized by translating the sample during the irradiation process. For applications using optical waveguides, this will be the first step: Generate a high refractive index core, surrounded by a lower refractive index, so that light can be confined.

The interest of DLW is that provided the material reacts to the high intensity of the laser and the writing parameters (wavelength, fluence, pulse energy), there

will be a refractive index modification that could be used for waveguiding, within the transparency window of the material. This gives a wide range of possibilities for single-mode waveguiding, from visible to mid-IR. As an example, the spectral domains of 3–5 μm and 8–12 μm are of great interest for astrophysical observation. Moreover, a large number of molecular organic tracers (water, CO_2, ozone) can be probed at these wavelength ranges. That gives the possibility to realize DLW devices for astronomical research of bio-signatures on exoplanets.

We present hereunder some examples of waveguide fabrication by DLW, to recall the type I or type II fabrications process.

1.1   Waveguides Based on Type I Modification

As an example of waveguide fabrication, we will show the fabrication of WG in commercial GLS glass (transparent up to 10 microns) and use a pulsed femtosecond laser to engrave the optical waveguides [26, 40]. The waveguides were fabricated using an ultrafast laser photoinscription technique described in [36]. GLS material is particularly interesting for laser photoinscription technique as it shows a large processing window of positive type I index changes. A multicore configuration is used to achieve large-mode-area guiding in the NIR and MIR with single-mode characteristics. This is based on a centered hexagonal arrangement of 37 parallel waveguides (and 5 μm radial separation between individual traces) with an index contrast in the range of 10^{-4}–10^{-3}. A view on the multicore waveguide structure and mode diameter at 1550 nm is given in Fig. 28.1. Injection in the central trace and evanescent coupling towards neighboring waveguides ensures coherent modal superposition [9, 55] and the formation and propagation of a single mode at this wavelength [36]. This allows to realize a large area mode, 22 μm FWHM, extending over the physical section of the waveguide.
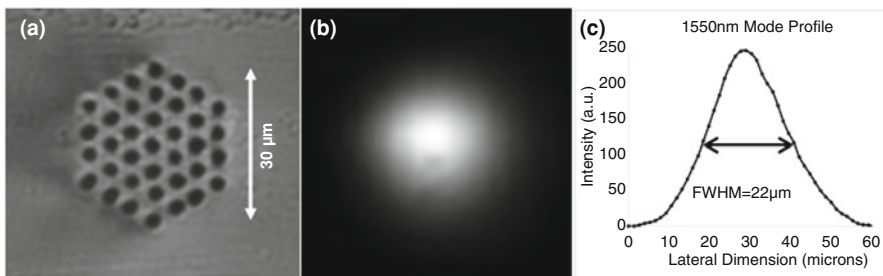

Fig. 28.1 (**a**) Multicore hexagonal single-mode waveguide fabricated in GLS using short laser pulses. (**b**) Image of the mode obtained using a 1550 nm SLED (same scale as (**a**)) and (**c**) mode profile showing large FWHM. (Reproduced from Martin et al. [36])
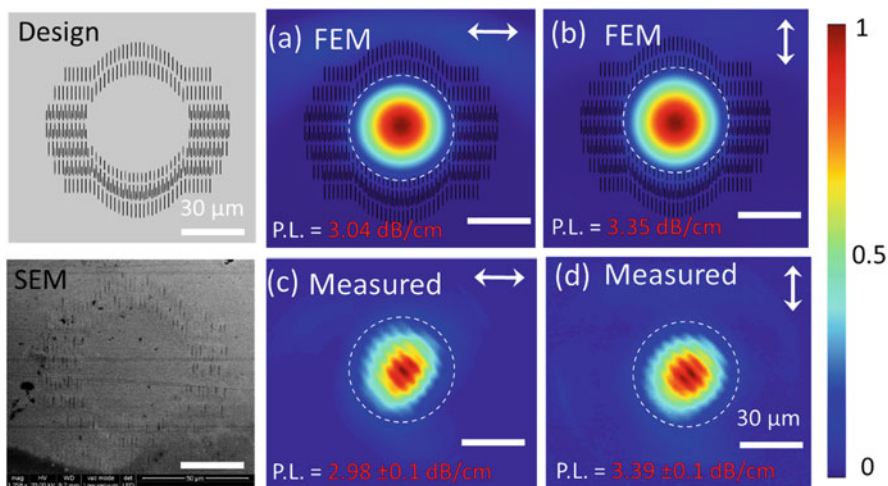
Fig. 28.2 Simulation and experiment of the type II laser-written waveguide: Comparison of near-field TE and TM modes. (**a**) FEM simulation for TE mode (resp. (**b**) for TM mode); (**c**) Experimental measurement of the TE mode (resp. (**d**) for TM mode). Interference fringes in the measured mode images are due to back-reflections in the optical guiding imaging system. (Reproduced from Nguyen et al. [42])

1.2 Waveguides Based on Type II Modification

In this approach, the laser fabrication involves the transversal inscription of tracks to construct a depressed-Δn circular array which supports leaky modes along the tubular channel [25]. Geometrical coordinates of each individual track were extracted from the 2D design and loaded to a script used in the laser inscription process. Trial of writing single tracks was initially conducted in order to specify the track sizes as a function of laser energy and focusing depth.

Using the refractive index profiles obtained [42], simulated TE and TM modes are compared with the measured mode fields, showing good dimensional agreement (Fig. 28.2). The FEM (Finite Element Method) design, obtained from the analysis of the SEM (Scanning Electron Microscopy) image of the cladding structure, is also shown.

Once the waveguide realization has been demonstrated, more complex structures can be investigated: Y junctions, tapers, interferometers (which can be useful for interferometry space observation), and optical sampling (for spectrometry applications). For that, high dielectric discontinuities must be generated using higher energy pulses. The strong interest of DLW relies here in the extension to the third dimension while keeping compact geometries, allowing for very complex and dense optical circuits and scattering centers.

2   DLW for Nano-sampling: Bessel Holes and 3D Antenna

In order to locally extract light from the confining waveguides, a dielectric discontinuity must be generated in the material, sufficiently small to not perturb the main function of the waveguides (confining and propagating light with low losses, without phase modification) but sufficiently contrasted so that enough light can be scattered and subsequently detected by a sensor (typically, a pixel/detector set on top of the waveguide). In order to generate this dielectric discontinuity using laser writing, a non-diffractive irradiation procedure [2, 3, 54] is used to generate a series of one-dimensional voids, transverse to the propagation axis of the waveguides, with a characteristic section below 500 nm and an axial dimension above of 150 μm. An overview of the optical device with side and top views is given in Fig. 28.3.

The main interest of laser writing for making the elongated nanovoids is that we can easily cover a sampling length of 1 cm, without mask replacement, in a very short time (few seconds). Besides, we can adjust the vertical position of the hole with respect to the waveguide, in order to optimize the extraction efficiency. The scattering efficiency depends on the cross-sections of the voids. For cross-sections between 100 and 500 nm and positions in the vicinity of the $1/e^2$ of the mode, scattering efficiencies ranging from 10^{-2} to 10^{-3} were estimated by FDTD calculations.

Using a single sampling center (here, a simple Bessel nanovoid) is of great interest if the detector is really close to the surface and has its active area, where the photon is absorbed, near the physical surface. Although this works properly for visible wavelength applications (CMOS detectors), it is no longer the case in near- and mid-IR (InGaAs, HgCdTe, or similar detectors), as the detector active area is hundreds of microns below the physical surface of the pixel. As seen in Fig. 28.4 [51], this will generate crosstalk and loss of flux detected by the pixel.
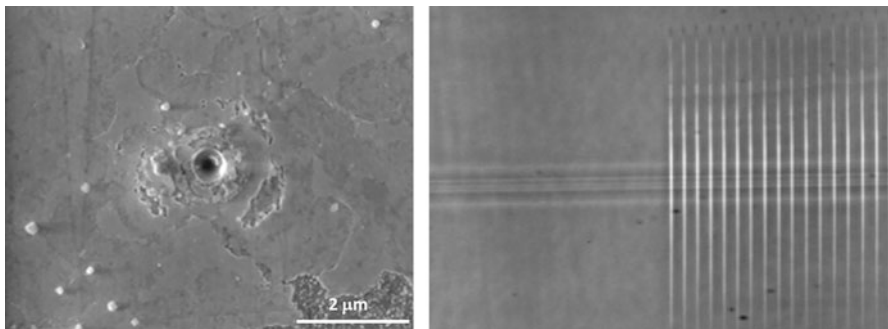

Fig. 28.3 Front view (left) of a Bessel void, using MEB imaging. Top view (right), using simple microscopy, of a set of Bessel voids transverse to the waveguide. (Reproduced from Martin et al. [35])
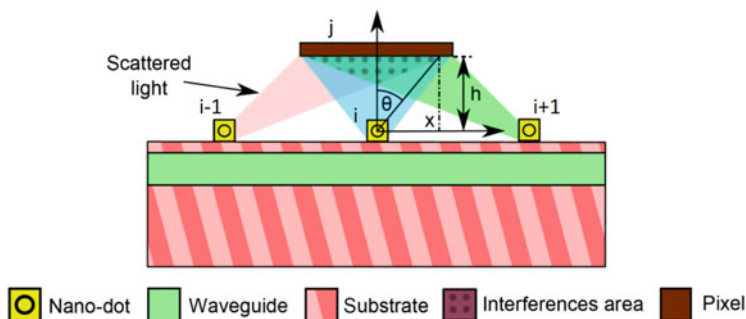
Fig. 28.4 Schematic view of the scattered light extracted from the sample and its angular divergence towards the detector, showing the problem of overlapping between too close sampling centers. (Reproduced from Thomas et al. [51])
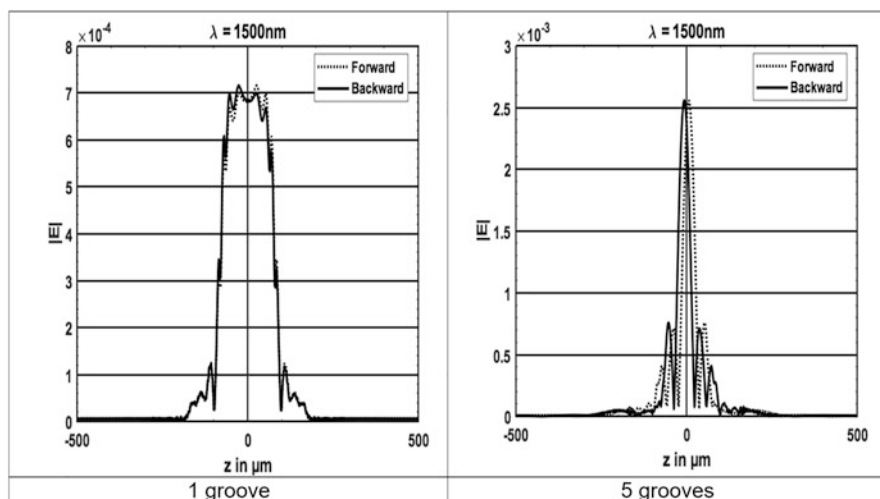

Fig. 28.5 Simulation of the scattered intensity profile issued from an antenna composed of N grooves at the optical wavelength 1500 nm. On the left for $N = 1$ and on the right for $N = 5$. (Reproduced from Bonduelle et al. [6])

An alternative method is to use the versatility of laser writing to inscribe several sampling centers to create a small diffraction grating on top of the waveguide. This way, the extracted flux will follow the laws of diffraction, allowing for higher directivity and narrow angular emission, optimally directed towards the pixel of interest, reducing crosstalk [41].

As seen in Fig. 28.5, the diffracted intensity is larger if we have a single groove, covering around 100 μm on the detector, meaning typical 5 pixels of 20 μm pitch. Therefore, in order to avoid crosstalk, one has to space the following antenna up to 100 μm, which means strongly reducing the spectral etendue. On the contrary, with more periodic grooves, the diffracted intensity is narrower, allowing for a more dense antenna distribution and an increase of the spectral etendue.

2.1   *Fundamental Law of Diffraction Using the Nanograting*

The first step to achieve a grating that will interact constructively with the optical beam inside the waveguide is to fulfill the following constraint: The spacing between scattering centers of our nanograting must be "in phase" with the optical beam, so that spacing $\Lambda = m \cdot \lambda/n$ with m an integer, and λ and n the wavelength and the effective refractive index of the guided mode, respectively. Of course, the lower the m value, the better, as sampling will be exactly coherent with the optical beam. Higher orders of m mean larger grating period and therefore angularly larger diffracted orders. Despite the performances of DLW, achieving $m = 1$ for $\lambda = 1.5\ \mu\text{m}$ and $n = 1.5$ (typical value in a borosilicate glass) means $\Lambda = 1\ \mu\text{m}$, which is a real challenge in terms of Bessel voids fabrication by DLW. We will focus on a grating using Bessel voids with a spacing of $\Lambda = 3\ \mu\text{m}$, a value that can be easily obtained with good repeatability.

The second step is to calculate the Bragg order created by the nanovoids, acting as a grating, in order to have the maximum diffraction angles that can be covered. The grating law gives us the number of expected Bragg orders in this case. Considering that the optical incident beam is perpendicular to the grating, the angular dependence is simply driven by the output angle, θ, such as:

$$n_{\text{sup}} \cdot \sin(\theta) = n_{\text{eff}} \cdot m \tag{28.1}$$

with $n_{\text{sup}} = 1.444$ (the superstrate refractive index); $-1 < \sin(\theta) < 1$; $n_{\text{eff}} = 1.446$ (the effective index of the guided mode); $\lambda = 1.55\ \mu\text{m}$; and $\Lambda = 3\ \mu\text{m}$.

From this we can deduce that $0.0039 < m < 5.5935$. As m can only be an integer, there are five diffraction orders. However, only three or four are clearly visible because of the total refraction between air and glass that rejects the orders arriving at higher angles. The simulation shown in Fig. 28.6a illustrates how the optical field, for a five-groove sampling center and a wavelength of 1550 nm, will be detected by the pixel array. It is also important to understand that the interaction between the grating and the waveguide is propagation sensitive, as the output angle of the diffracted beams is either positive or negative, depending on the beam propagation direction, either forward or backward, as presented in Fig. 28.6b.

Although a 3 μm grating spacing is not ideal, we can extract some information on the directivity and extraction efficiency of the system. The experimental set-up for the study of the vertical radiation pattern is the following: an IR camera is placed on the sample, above the sampling centers and waveguides. This camera is chosen because its pixel matrix can be uncapsulated, allowing to set the matrix directly in contact with the sample, reducing the light's vertical path. The experiment consists in measuring the radiation pattern for different heights of the camera: First the camera is in physical contact with the sample, and then it is raised step by step from $h = 0$ to $h = 520\ \mu\text{m}$.

In Fig. 28.7, we can observe that depending on the number of grooves (number of nanovoids forming the diffraction grating), the diffracted flux varies from an
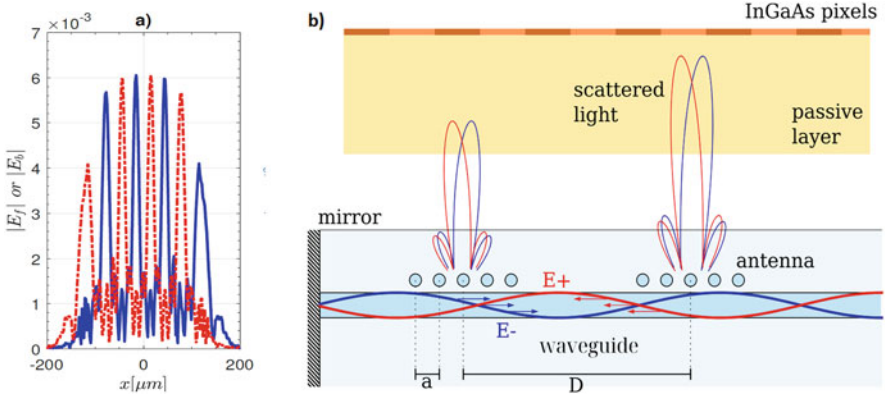
Fig. 28.6 (**a**) Superposition of the incoming wave only (red) and the returning wave (blue) on the pixel array. This figure shows the expected Bragg orders and how they overlap: the signal is not symmetric, and there is a slight angular offset between the incoming and returning wave. (**b**) Sketch of the radiation pattern from two consecutive gratings, as a function of the direct (red, E+) and backward (blue, E−) propagating beams in the waveguide. Depending on the wavelength and the refractive index, the diffracted angle will determine how the direct and backward beams overlap on the pixel array
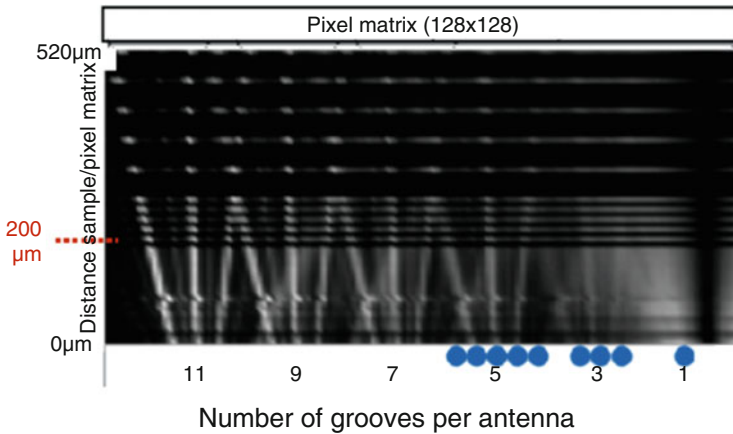

Fig. 28.7 Evolution of the vertical radiation pattern as a function of height between the detector and the sampling center, for different numbers of grooves per diffracting antenna

angularly large and diffused emission cone (for a single groove) to a narrower angle and flux concentrated on the specific Bragg diffraction orders (for 11 grooves), improving the directivity and extraction efficiency. Indeed, having a larger number of grooves not only improves the angular directivity, but it also increases the total extracted flux and, therefore, the signal-to-noise ratio. Let us note however that in the ideal situation (perfect matching $\Lambda = \lambda/n$), only one Bragg order is expected, gathering all the sampled signal, and directed towards a unique pixel.

2.2   Spectral Dependence on the Extraction Efficiency

One of the features of these gratings is that the output angular direction is dependent on the wavelength (see (28.1)). Considering that light injected in the waveguide makes a backward beam by reflection on the opposite surface, this implies that the flux extracted from direct and backward beams will overlap, generating interference fringes on the detector. The contrast of this fringes is related again to the wavelength and the total phase mismatch between the direct and backward beams, resulting in a spectral signature that can be used to make accurate spectrometry.

In Fig. 28.8 [6] is shown the simulated intensity detected on the pixel, as a function of the wavelength, for the total optical field extracted from the grating (interference between the direct and backward beams). As seen in the graph, with the increasing number of Bessel nanovoids in the grating, the measured contrast becomes more selective to wavelength.

As seen in the left column of Fig. 28.8, the fringe intensity changes following the optical wavelength used. From the interference fringes, two envelopes are calculated: the envelope of the fringe minima and the envelope of the fringe maxima. From both envelopes, the fringe contrast is then calculated. Increasing the number of grooves reduces the bandwidth of the high contrast fringes (i.e., good spectral sensitivity). This feature will be used to determine an unknown wavelength and use the global system coupling an optical waveguide and the grating as a lambdameter.

We have shown the interest of DLW to generate Bessel voids that allow to extract the signal from a waveguide and improve its directivity towards a detector. We are now going to explore more in detail the principle of spectrometry using DLW for fabrication of the waveguide(s) and the number of nanovoids and nano-gratings needed to achieve high-resolution spectrometry on-chip.

3   Stationary Wave Fourier Transform Spectrometry: SWIFTS

The principle of SWIFTS [31] is based on the generation of a stationary wave inside an optical waveguide and the nanoscale sampling of this stationary wave in order to obtain a discrete interferogram from which, using discrete Fourier transform, the spectrum of the signal is reconstructed. The aim of this section is to show how the DLW Bessel nanovoids are used to periodically sample the signal in the waveguide. Two configurations are proposed: the stationary waves are obtained either from a guided mode being reflected at the opposite facet from the injection (Lippmann mode, Fig. 28.9, right) or from two counterpropagative mode interference (Gabor mode, Fig. 28.9, left).

In the simplest configuration (Fig. 28.9, right), light is coupled into a single-mode waveguide terminated with a mirror. The superposition of the forward wave with the backward wave issued from the mirror reflection gives a stationary wave.
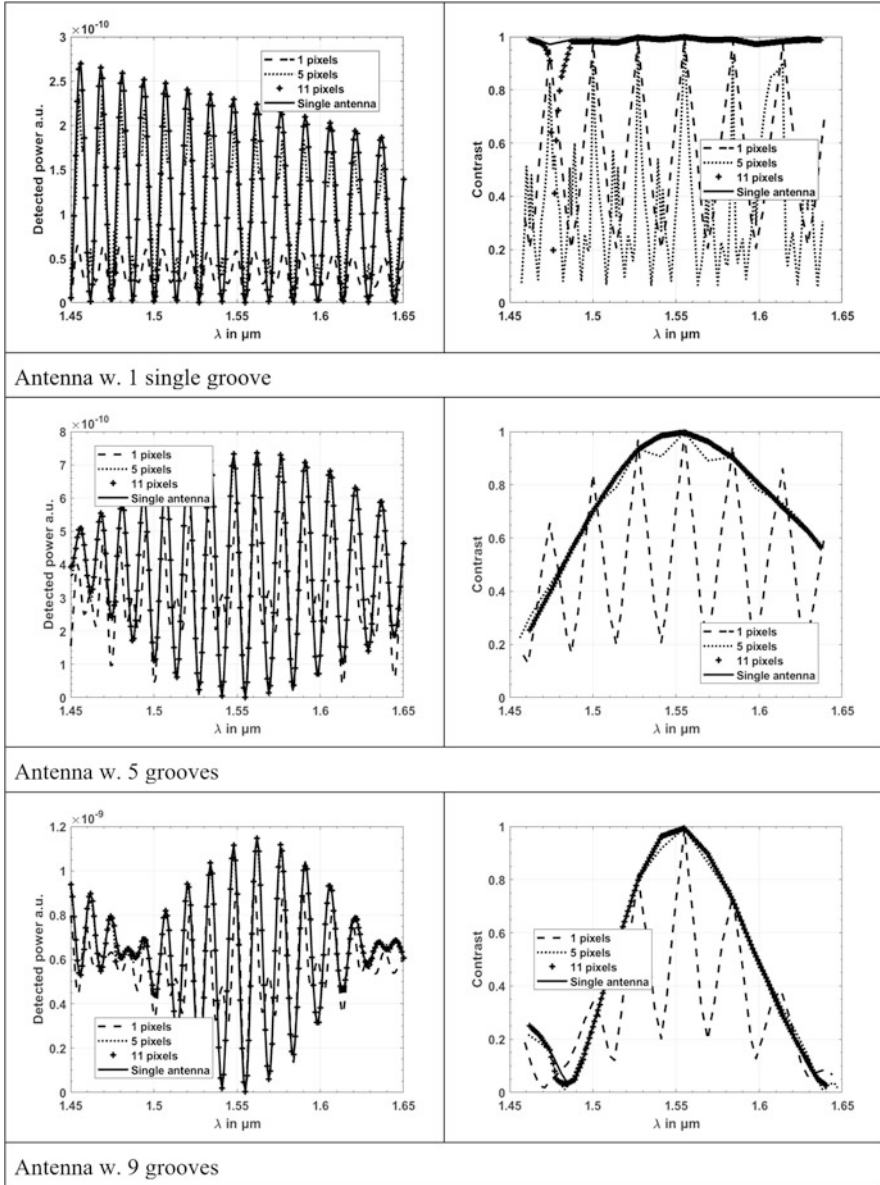
Fig. 28.8 Trade-off between extraction efficiency and spectral band for high fringe contrast, for three types of antenna, depending on the number of grooves used in one antenna (1, 5, or 9, respectively). On the left, the detected power as a function of wavelength. On the right, the contrast of the fringes. The inset means 1 pixel = an antenna every 20 μm; 5 pixels = an antenna every 100 μm, and 11 pixels = an antenna every 220 μm. Single antenna means integration over the whole detector for a single antenna (ideal case). Therefore, increasing the pixels' spacing improves the contrast and sensitivity spectral range. (Reproduced from Bonduelle et al. [6])
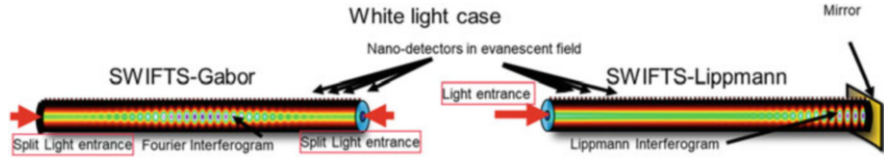
Fig. 28.9 Different configurations to obtain a static interferogram inside an optical waveguide: Left, counterpropagative configuration (Gabor mode); right, Lippmann mode, using reflection at the output facet of the sample. The fringes are sampled using nano-scatterers on the evanescent field of the optical guided mode, generally on top of the waveguide

Miniature localized detectors are placed in the evanescent field of the waveguide mode in order to extract only a small fraction of the guided energy. This peripheral detection approach allows proper sampling of the standing wave using relatively small size detectors in comparison with the quarter wavelength of the guided light. The interferogram resulting from white light illumination is called Lippmann mode. Unlike a classical Fourier interferogram, Lippmann's interferogram starts at the surface of the mirror with a null optical path difference fringe such that only half of the fringe packet is detected. In this way the whole energy is recovered using a minimum number of detectors. This principle thus acts like a spectrometer with simultaneous recorded Fourier transforms, i.e., no moveable part is required to record the information needed to restore the spectrum. However, the drawback of this system is that the interferogram is folded, as seen in the Lippman mode in Fig. 28.9, right so that any asymmetric spectral information (i.e., relative chromatic dispersion) is hidden in the full wideband packet and will be averaged with the Lippmann configuration.

The second SWIFTS configuration (Fig. 28.9, left) is based on the same near-field detection idea, but instead of using a mirror, the light is injected from both sides of the waveguide, and it is known as Gabor configuration. A similar configuration has been proposed by Labeyrie et al. [29] for a data storage system which is an extension of holography [12, 21] or of a Sagnac interferometer [46]. In this configuration, the resulting interferogram is a typical full Fourier interferogram which, in contrast with the mirror configuration, is sensitive to the optical path difference. This type of spectrometer could therefore also be used in metrology.

The interest of SWIFTS spectrometers is their compacity and robustness, as they do not require any relay optics, with the detector directly glued on top of the surface, as shown in Fig. 28.10 (left).

3.1 Principal Equations of the SWIFTS Spectrometer

The main equations of the SWIFTS spectrometer [31] state that the spectral resolution SR is related to the sampling length L and the refractive index (or more exactly, the effective index of the guided mode, n) by:

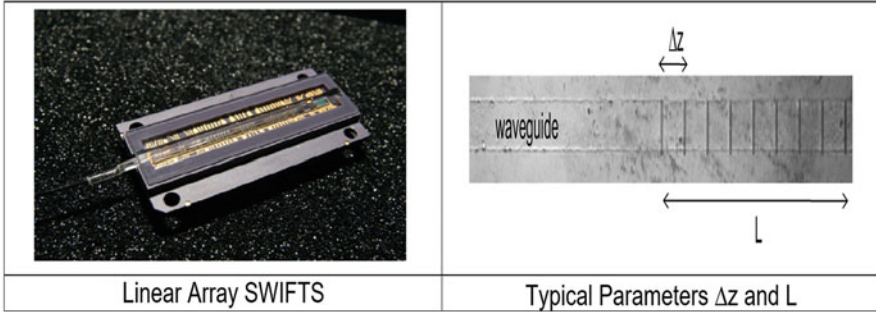| Linear Array SWIFTS | Typical Parameters Δz and L |

Fig. 28.10 Left: Image of a visible commercial SWIFTS interferometer, showing the optical waveguide (fed by an optical fiber) glued directly to the CMOS linear detector. Right: Image of a waveguide with nano-grooves on the surface, showing the typical parameters of the sampling region (L = total sampling length and Δz = sampling period)

$$\text{SR} = 2\ nL/\lambda \tag{28.2}$$

And that spectral étendue (or spectral range) before aliasing is related to the sampling period (distance between two sampling centers, Δz, see right part of Fig. 28.10).

$$\Delta \lambda = \lambda^2/4n\,\Delta z \tag{28.3}$$

To have an idea of the orders of magnitude, an example is given for a glass waveguide: $L = 1$ mm, $\lambda = 1.55$ microns, and $n = 1.44$, a spectral resolution of SR = 1858 is obtained so that resolution is rapidly several thousands and the spectral range is $\Delta \lambda = 41$ nm for $\Delta z = 10$ μm, which is a typical pixel pitch. This means that one could expect a thousand resolution in a 1-mm-long sample, with a spectral window of 41 nm, which is sufficient for many applications.

However, in order to expand the spectral range and correctly sample the signal, one has to fulfill the Shannon-Nyquist criteria. If we focus on the Lippmann configuration [50], the intensity equation relating the intensity along the waveguide to the distance to the mirror is:

$$I\,(\lambda, z) = I_0 \left[1 + R - 2\sqrt{R} \cos \left[\frac{4\pi}{\lambda} n_{\text{eff}}\,(\lambda)\,z \right) \right] \right] \tag{28.4}$$

where z is the distance from the waveguide output facet, n_{eff} is the effective refractive index, and I_0 is the input intensity. Also, R is the reflectivity of the mirror, typically $R > 90\%$ (in case we do not use a mirror, this value is simply the Fresnel reflectivity of the material for a perpendicular incidence, $R = ((n-1)/(n+1))^2$). This value can be strong enough to achieve the SWIFTS effect for high refractive index materials such as lithium niobate. Indeed, with $n = 2.2$, $R = 13\%$ can be reached without any technological step for mirror deposition in the output facet.

Knowing that the interferogram has a period of λ/2n, with λ the wavelength and n the refractive index, the sampling period has to be inferior or equal to λ/4n in order to avoid aliasing. This value is therefore the maximum distance that we can have between two sampling centers (two antennas). For a typical borosilicate glass, with a refractive index around 1.444 at λ = 1.55 μm, the maximum period allowed between two sampling centers is $\Delta z = 268$ nm. This small dimension between sampling centers is not achievable with ultrafast laser writing. But even using complex nano-lithography, the limit of sampling period is the size of the pixel or pixel pitch, which is typically tens of microns. Therefore the stationary wave will necessarily be under-sampled, resulting in a reduced spectral range, typically tens of nanometers for typical pixel pitch of 10 μm. Note that this is not a drawback for laser characterization, where a high resolution is needed over a very narrow window. However, for wide-range spectroscopy (atmospheric detection, mid-infrared molecular analysis, etc.), large bandwidths are required. In order to solve that problem, a phase shift modulation, spatial or temporal, can be introduced. Before exploring these solutions more in detail, let us try to understand the behavior of the static interferogram and the intensity extracted by the DLW grooves, as a function of distance to the mirror, and wavelength, to understand the spectral signature of the signal.

3.2   Dependence of the Signal with the Wavelength and Distance to the Mirror

In (28.4) it can be seen that the intensity along the waveguide depends on the distance z from the waveguide output facet, where reflection occurs and the Lippmann interferogram starts. This dependency can be exploited to make a first simple wavelength meter: Using DLW, we fabricated a set of waveguides, with six antennas [5]. Each antenna consists of five nanovoids, with 3 μm spacing, and each antenna is 400 μm further from the previous one, the first being at 400 μm from the mirror (sketch shown in Fig. 28.11).

As can be seen in Fig. 28.11, the furthest the antenna is from the mirror, the more rapidly the signal oscillates as the wavelength varies (in this case, from 1560 to 1565 nm), being therefore very sensitive to wavelength variations. In order to study the results given by the sample, a high-resolution database is created, consisting on a full scan using a Tunics tunable laser source, between 1510 and 1600 nm, with a wavelength step of 50 pm. The detected intensity of a line of pixels along the six antennas is recorded as a function of wavelength, obtaining a 2D map (see Fig. 28.12).

Then, using this data base as a reference, an unknown wavelength issued from the same source was injected in the sample, and its expected value was retrieved through a comparison algorithm (least squares values search). As an example, the
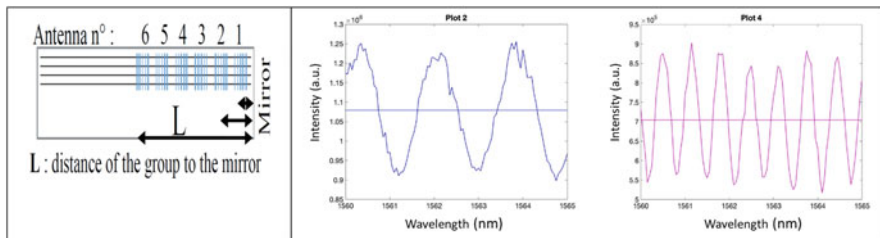
Fig. 28.11 Sketch of the fabricated sample, showing different sets of nano-scattering centers (Bessel voids) at different distances from the mirror. All scattering centers consist of five Bessel voids, to improve flux directivity. On the right, the sampled intensity for antennas number 2 and 4, respectively, showing the influence of the distance to the mirror on the frequency of the fringes. (Reproduced from Bonduelle et al. [5])
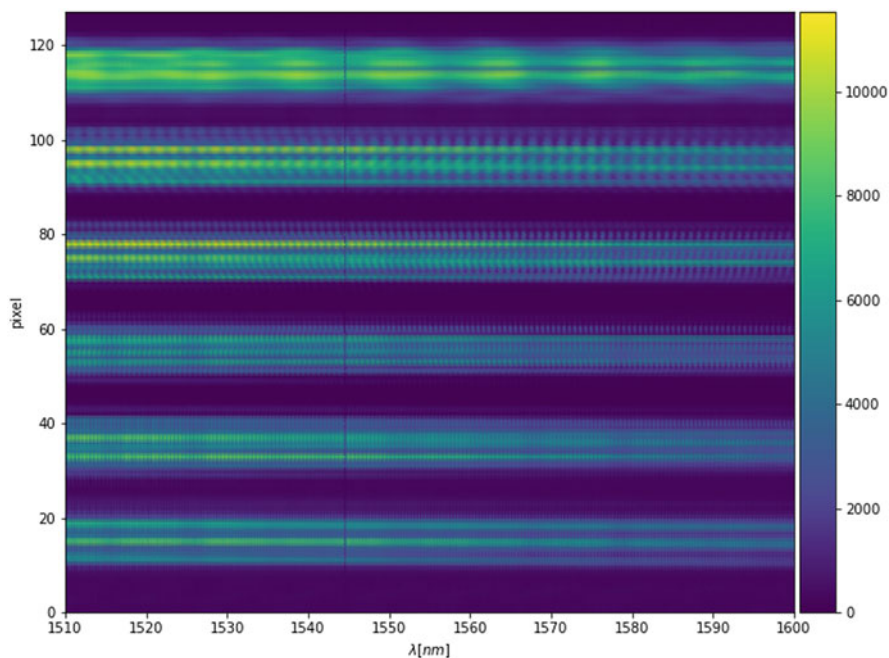

Fig. 28.12 Intensity recorded over each of the antenna while scanning the wavelength from 1510 to 1600 nm with 50 pm step. The top signal comes from the first antenna (closest to the mirror), and the bottom signal comes from the sixth antenna (furthest from the mirror)

recovery of an unknown wavelength, within the spectral window of the system, is shown below.

These results show that the unknown wavelength can be determined with a high accuracy, around 25 pm. However, as seen in Fig. 28.13, there can be two local minima that do not give the same result because of aliasing (secondary guess at
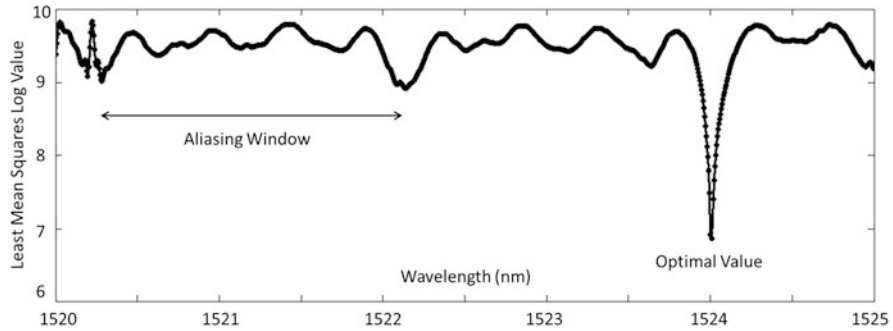
Fig. 28.13 Result of a least squares search for an unknown wavelength (1524.03 nm) injected on the system and comparison with the database (1524 nm), allowing for a guess wavelength with an accuracy around 25 pm

1522.3 nm). However, the global minima is still the accurate one, and the unknown value can still be retrieved.

We are now going to explore how to increase the spectral etendue and work towards the development of large spectral band spectrometers.

4   Laser-Written SWIFTS in Passive Materials: Spatial Multiplexing

As it has been shown in Sect. 2, the main drawback of the SWIFTS approach to spectrometry is that sampling must be done at λ/4n at least, which means hundreds of nanometers between sampling centers, which is not possible actually with commercial detectors. In order to reach a better spectral etendue, a first possibility is to use parallel waveguides where the same interferogram is encoded, but use the accuracy of laser writing nano-scattering fabrication, to set the sampling centers with a spatial shift in each waveguide, so that different parts of the interferogram are sampled. After stitching, the high-density sampling interferogram is recovered.

An example of spatial offset obtained by sampling the wave using several waveguides rather than a single one and introducing a spatial shift is given in Fig. 28.14.

Each waveguide has its own set of sampling centers, with the same spacing but shifted in comparison to the other waveguides. In the example of Fig. 28.14, the shift between each antenna is ¼ of the spacing between two antennas, therefore using four waveguides to complete the set. A fifth waveguide is prepared to check redundancy with the first one. This scheme can be of course increased to a $1/M$ shift, needing M parallel waveguides to work. We will discuss on this later on this chapter, as it raises the problem of how to inject light into M single-mode waveguides simultaneously.
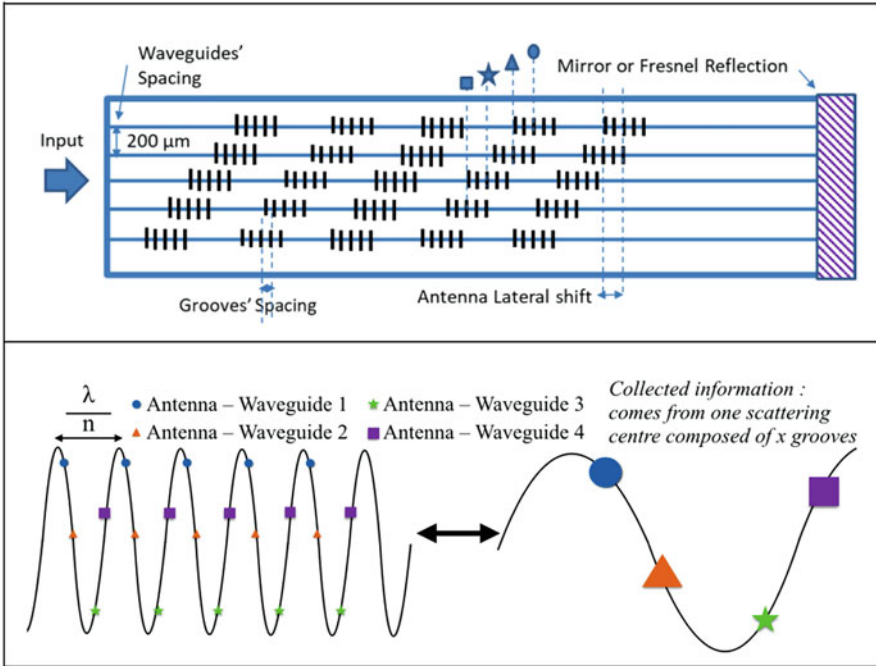
Fig. 28.14 Sampling with a spatial offset. Each antenna is set at a different length from the reflecting mirror, sampling a different part of the interferogram. After stitching, an improved sampling of the interferogram is obtained. (Reproduced from Bonduelle et al. [6])

With the multiplexing of the four first waveguides, the sampling can be correctly done (i.e., four sampled values for one optical period).

The numbers are very easy in this case: Increasing to M waveguides implies a increasing of the spectral range by $M \cdot \Delta\lambda$, where $\Delta\lambda$ is still directly related to the spacing Δz between two consecutive antennas in a given waveguide. It is important to note however that as the waveguides have to be single mode, if we want to keep an integrated optic system, one needs a way to inject light to the waveguides simultaneously. This can be done using a photonic lantern that can be also fabricated using DLW [4, 52], followed by the straight parallel waveguides containing the shifted sampling centers (see Fig. 28.15).

The interest of spatial multiplexing is that the signal can be obtained in a single measurement; however, it implies a collecting multimode waveguide and a perfect control of the transition between a (multi) M-mode waveguide to M single-mode waveguides.

Note that an alternative to spatial shift, if increasing the spectral range is not needed, is to keep the photonic lantern for high-efficiency light collection (thanks to its multimode, high numerical aperture behavior) and set the M parallel waveguides with exactly the same position for sampling centers. Therefore, with this square,
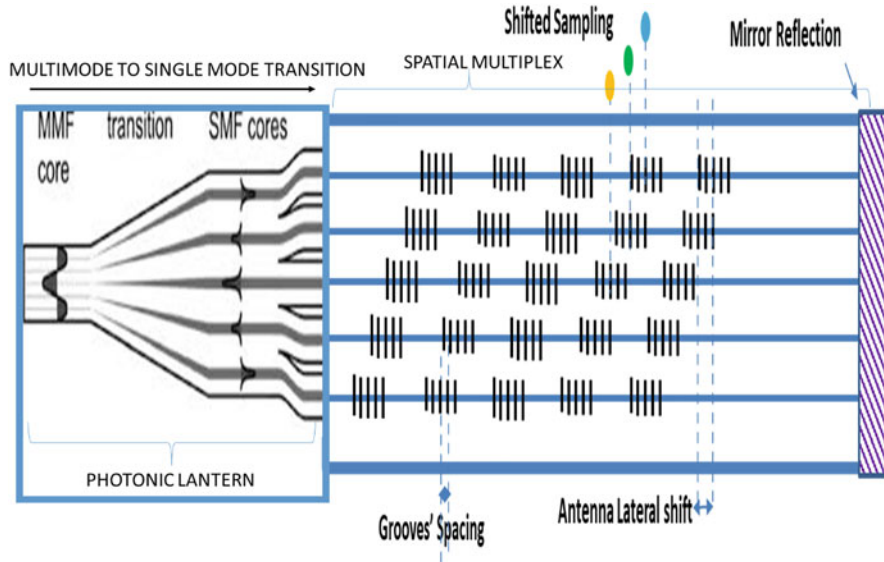
Fig. 28.15 Basic principle of a spatial multiplexer based on a collecting photonic lantern (image extracted from [4]), followed by a set of parallel waveguides with the shifted sampling centers

pixel matrix, one can increase the signal-to-noise ratio, as the signal is distributed between M theoretically identical waveguides and noise can be averaged.

5   Laser-Written SWIFTS in Active Materials: Temporal Multiplexing

An alternative configuration to simplify the system is to fabricate a single-mode waveguide in a material that could observe a phase shift under an external perturbation such as temperature or electric field. With this approach, only one waveguide is needed; therefore the fabrication complexity reduces (no need of photonic lantern or multiple waveguides), and the cost of the detector is lower (no need of 2D matrices, only an array, and eventually, only a single pixel is needed).

As shown in (28.4), the intensity along the waveguide is related to the effective index of the guided mode. If we have a way to vary its value, using a physical property of the optical material, then we are able to temporally shift the fringes under the extracting antenna and, therefore, scan the fringes of the interferogram. However, in order to obtain the temporal shift of the fringes under the detector, it is compulsory to have a relative optical phase modulation between two interacting fields. The intensity along the output waveguide is then given by [33]:

$$I\left(z, \delta\right) = 2I_0 \left[1 + \cos\left(\frac{2\pi}{\lambda} \Delta n\left(\delta\right) L_{\text{elec}}\right)\right] \left[1 + R - 2\sqrt{R} \cos\left[\frac{4\pi}{\lambda} n_{\text{eff}} z\right]\right]$$

$$(28.5)$$

As seen in (28.5), the SWIFTS interferogram (right part of the equation) is now coupled to an active modulation term (left part of the equation) that will help us to achieve the desired temporal shift. Two possibilities are going to be presented in the following sections.

5.1 The Electro-Optic Approach

One possibility is to explore the Pockels effect, which occurs in some particular crystals. This electro-optic effect [47] implies that the refractive index of a material (and, therefore, the effective index of the guided mode in a waveguide) can vary under the application of an electric field.

A typical configuration, using the most used electro-optic crystal (lithium niobate, $LiNbO_3$), gives a typical dependence of the refractive index with the electric field E_z such as:

$$\Delta n_{zz}(E) = -\frac{1}{2} n_{zz}^3 r_{zzz} E_z = -\frac{1}{2} n_e^3 r_{33} E_3 = -\frac{1}{2} n_e^3 r_{33} \frac{V_{\text{app}}}{d_{\text{elec}}} \qquad (28.6)$$

This variation Δn is to be introduced in Eq. (28.5), to understand the intensity variation seen by the pixel above the scattering center. When a voltage ramp is applied, we can scan the fringes, obtaining typically the signal shown in Fig. 28.16.

If several scattering centers are set along the waveguide, as the voltage ramp increases, the wide band fringes will shift from one center to the next one (as shown in Fig. 28.17, left), allowing for a temporal stitching and further reconstruction of an interferogram with increased spectral range (Fig. 28.17, right). An example of a SWIFTS electro-optic spectrometer can be found in [33].

This idea is currently being explored by developing DLW in lithium niobate to achieve simultaneously the waveguides and the scattering centers and, in a second step, fabricate the electrodes. Preliminary results on the waveguides and the nano-gratings are shown in Fig. 28.18.

Preliminary results show that the refractive index contrast between the grooves and the waveguides are not strong enough to allow for efficient optical sampling. A new set of samples, with modified parameters and increased laser writing energy, is being studied.
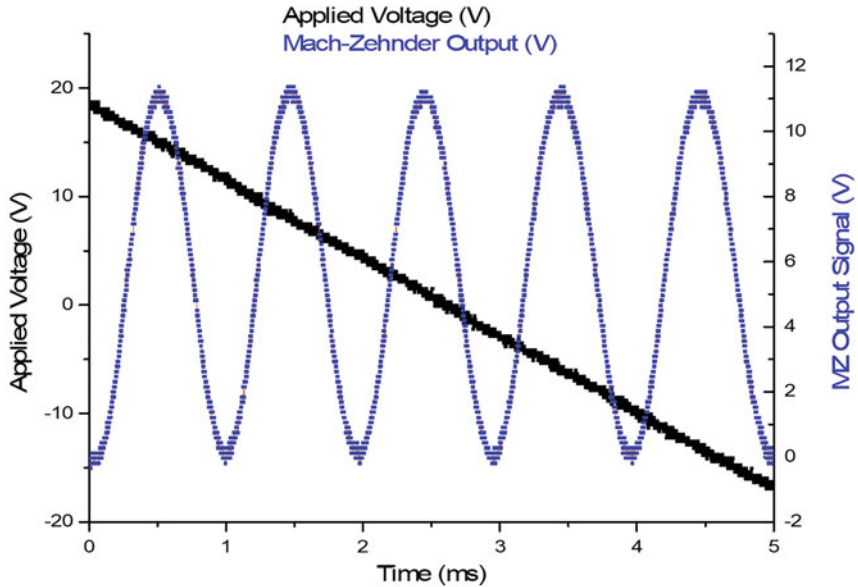
Modulation Freq 100Hz ; Voltage 34.32V ; Offset 0.44V ; Wavelength 2.2μm

Fig. 28.16 Demonstration of the intensity modulation under an applied electric field in a Mach-Zehnder modulator
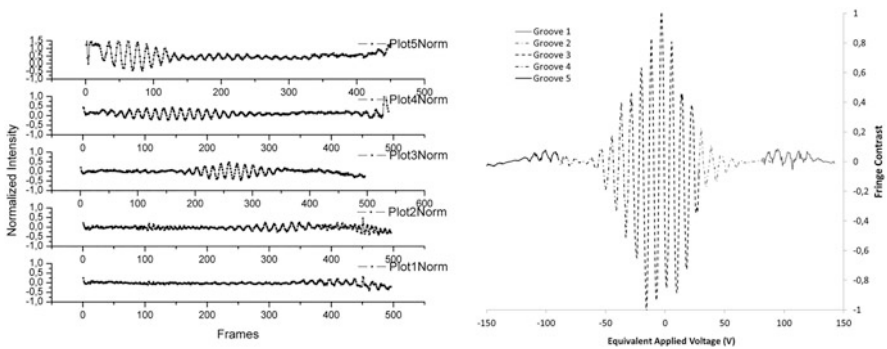

Fig. 28.17 Example of a temporal phase shift introduced in a lithium niobate SWIFTS. The wide band fringes are shifted from a sampling center to the next, thanks to an applied voltage, allowing to reduce the effective sampling step and therefore increasing the spectral range. (Reproduced from Loridat et al. [33]). Note that the source must present a limited coherence length, so that an envelope can be found to identify the relative phase between scattering centers and achieve the stitching
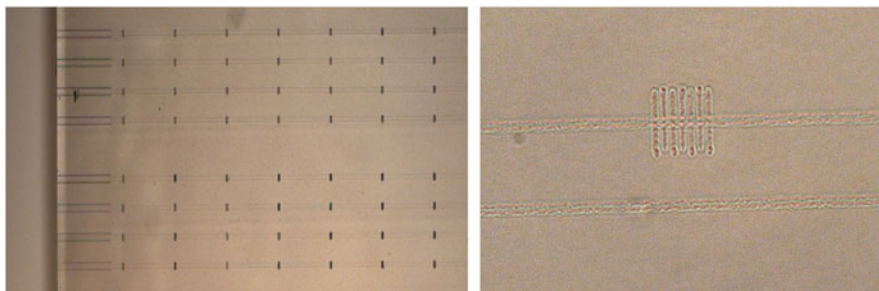
Fig. 28.18 (*Left*) Image of a set of parallel waveguides fabricated by DLW in lithium niobate, with the sampling centers (sets of nano-grooves) also fabricated by laser writing at the Univ. of Salamanca (J. R.V. de Aldana), on the surface of the sample. (*Right*) Zoom on a sampling center showing the seven nano-grooves on top of the waveguide
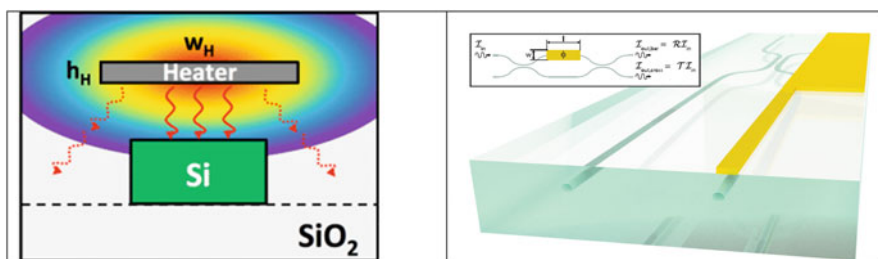

Fig. 28.19 (*Left*) Principle of the micro-heater, showing how the top electrode will diffuse heat through the Joules effect induced by the strong current passing through the metal. (*Right*) Example of a DLW thermo-optic beam coupler. (Reproduced from Ceccarelli et al. [8])

5.2 Thermo-optic Effect

A second approach is to actively modify the refractive index by locally changing the temperature of the waveguide. The thermo-optic effect is again related to the thermal constants of the material, but has the interest of being in principle available for any material (glass or crystal), as soon as its thermal constants are strong. Compared to the electro-optic effect that is limited to crystals (not glasses), and only for not-centrosymmetric crystals, the thermo-optic effect can offer a wider range of materials for testing.

The principle is based on the heating of the metallic wire on top of the waveguide (Fig. 28.19 left), resulting from a high current passing through. This will in turn generate a local increase of temperature and, subsequently, the modification of the refractive index of the waveguide, resulting in a phase shift that can be used for intensity modulation (Fig. 28.19 right). Thermal shifters have been demonstrated for several integrated photonics technologies, like silicon photonics [23, 56], silica-on-silicon [37, 39], and, more recently, also for platforms based on DLW of waveguides in transparent substrates [8, 18, 19].

As seen in this section, the advantage of temporal modulation is to call for simpler waveguide and detection construction, but needing more lithographic steps in order to set the electrodes or heaters. Besides, the signal is constructed by temporal phase-shifting, so that there is no snapshot measurement.

6 Perspectives: Image Reconstruction, Spectro-Imaging, and Wavefront Sensing

We have focused on a particular approach for laser-written spectrometers based on the SWIFTS principle. Of course, as long as the laser writing process allows for local modification of the refractive index, and accurate alignment of the laser is achieved to cover large surfaces, one can imagine many other approaches. We will present some of them hereunder. The main driver for the examples shown below is the possibility to achieve spectro-interferometry, that is, to obtain interference fringes from two or more optical inputs (typically astronomical telescopes) and span these fringes as a function of the wavelength to get access to the fringe contrast as a function of wavelength. Two applications are driving these concepts: phase closure studies [44] and image reconstruction using sparse aperture masking [10]. We will discuss this in Sect. 6.3, after briefly presenting two other approaches to spectrometry using direct laser writing.

6.1 Arrayed Waveguide Gratings

Arrayed waveguide gratings (AWG) are based on the concept proposed by Smit and Van Dam [48]. The heart of the system is a set of waveguides with an optical path length that is gradually increased, resulting in an output where different wavelengths superimpose at different lateral positions of a planar output waveguide, obtaining directly the spectrum along the horizontal axis of the sample, as shown in Fig. 28.20. These systems proposed initially in classical waveguide technologies (lithography), have been developed using DLW [14].

The example shown in Fig. 28.21 [16] proposes a horseshoe layout [15, 17]. The input waveguide is single mode at 633 nm and connects to the center of the first FPZ (free propagation zone). The FPZ (7.7 mm × 0.9 mm) confines the light in the vertical direction while allowing it to diffract in the horizontal direction. At the output of the FPZ, 0.7-mm-long linear adiabatic tapers guide the light into an array of 19 single-mode waveguides. Each waveguide has an incrementally longer optical path length (for this design $\Delta L = 11.77$ µm), with an average length of 12.55 mm. At the end of the waveguide array, linear adiabatic tapers allow the mode size to increase. Light is then recombined in the second FPZ, creating a horizontally dispersed spectrum of the input signal at the output of the chip. More details on the
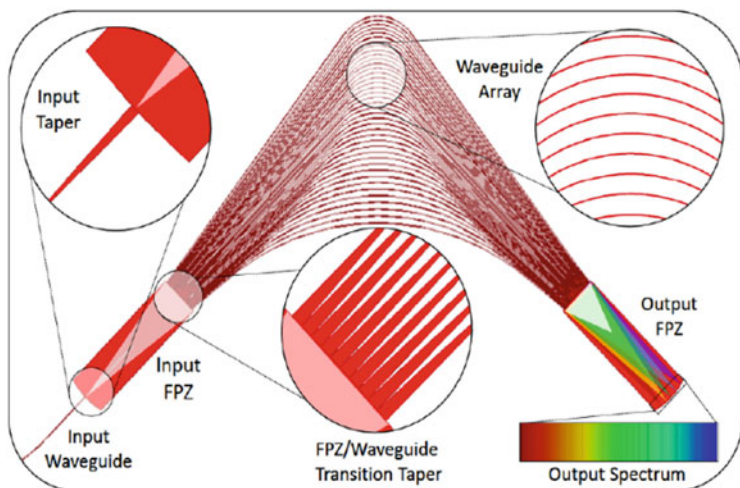
Fig. 28.20 Principle of an arrayed waveguide grating. (Reproduced from Douglass et al. [14])
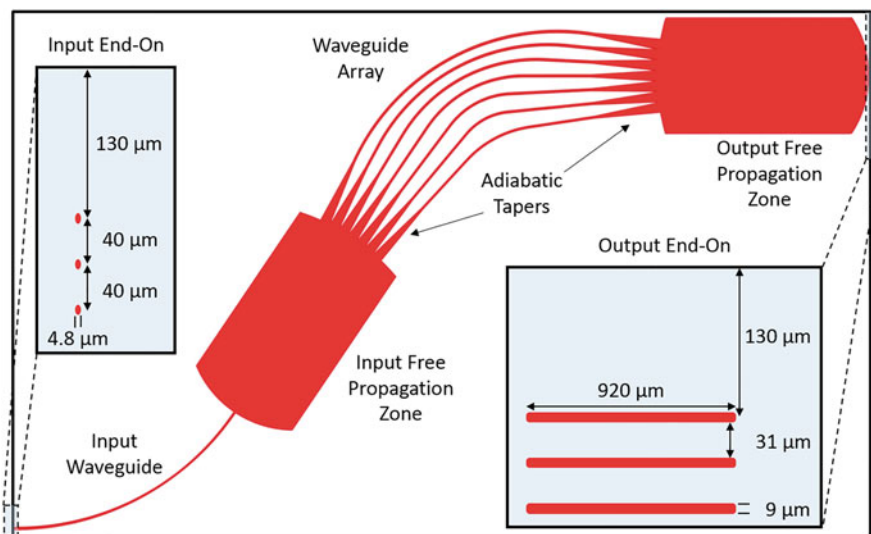

Fig. 28.21 Top-down schematic of a three-layered AWG sample. Inserts show the input and output end-on. (Reproduced from Douglass et al. [16])

principle of these AWGs can be found in [15, 16]. In order to achieve interference between different inputs, three identical AWGs were stacked vertically separated by 40 µm at three depths 210, 170, and 130 µm. A vertical spacing of 40 µm (center-to-center) was chosen to avoid coupling between AWG layers.

A bright-field microscope image of a tri-layered AWG output facet is shown in Fig. 28.22 (*left*). The thickness of each modification layer is 9 ± 0.2 µm,
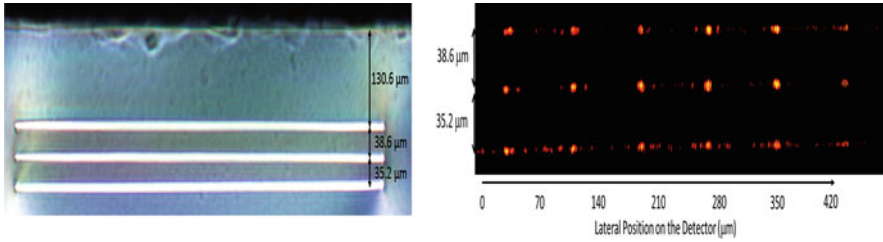
Fig. 28.22 (*Left*) White light image of a tri-layered AWG output facet. (*Right*) Output image of the diffracted modes, for the three layers injected simultaneously, at 790 nm. (Reproduced from Douglass et al. [16])
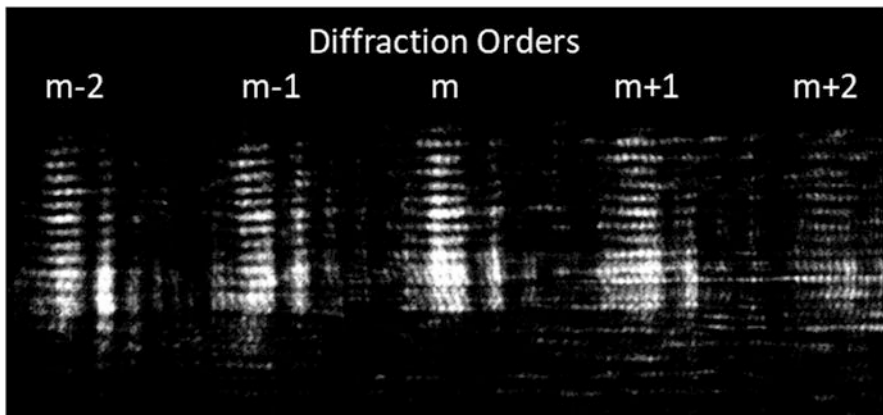

Fig. 28.23 Vertical superposition of the output orders, when the signal is defocused on the detector. (Reproduced from Douglass et al. [16])

which compares well to the designed 9 μm. The spacing between each AWG layer is 35.2 μm (lowest-center) and 38.6 μm (center-highest), which is smaller than the designed spacing of 40 μm. This is due to spherical aberrations affecting the modification depth. All three AWG outputs are 920 μm wide. A previously fabricated AWG with the same design had a measured throughput of 11.5 $\pm$ 0.2% at 635 nm across 5 orders [15]. As the wavelength is increased, the throughput was found to decrease due to material absorption.

The three AWGs were tested simultaneously using a near IR Sacher tunable laser centered at 790 nm. The output of the stack of AWG is shown in Fig. 28.23. As the modes are properly arranged vertically, one can play with defocusing, in order to obtain vertical superposition of the flux coming from the waveguides.

We can thus recover the vertical fringe contrast as a function of wavelength, which is the observable we are looking for.

6.2 Far-Field Spectrometers

Another approach is to fabricate several parallel channel waveguides, extract the light from them, and make it interfere, so we can obtain a spectro-interferometer. We fabricated a set of four large-mode-area channel waveguides ([9, 40, 55]; d'Amico 2014) aligned in a plane, with a center-to-center separation of 250 μm, and buried at 800 μm from the surface. In a second step, a non-diffractive irradiation procedure [2, 3] was used to generate a series of one-dimensional voids, transverse to the waveguides, with a characteristic section below 500 nm and an axial dimension above 150 μm, separated by 30 μm (see Fig. 28.24).

Here, as the sampling centers are fabricated inside the material, a symmetric radiation pattern is expected, resulting in a more efficient flux extraction towards the surface. In order to efficiently recover the flux, and discriminate eventually different order modes, we have developed a simple set-up using a cylindrical lens for collecting the wide angle flux and focus different wavelengths at different pixels and a second optical stage to reduce aberrations, disperse laterally diffraction modes, and avoid overlapping.

In order to check proper injection into the waveguides, an image of the waveguide output is obtained on the FLIR camera (Fig. 28.25a) and from above using a simple microscope objective (Fig. 28.25b).

Vertical characterization of the extracted signal (Fig. 28.26, inset B) is achieved using a three-cylindrical lens tube (Fig. 28.26), allowing to image the diffracted signal from the nanovoids to be detected on a Goodrich near IR camera. With this optical set-up, L2 and L3 focus different wavelengths at different areas on the CCD (Fig. 28.26, inset A), along the direction of the channel waveguide.

The equation of the system couples the refractive effective index of the propagating mode, n_{eff}, with the period of the sampling centers Λ and gives the output angle θ as a function of wavelength:

$$n_{\text{eff}} - n_{\text{ext}} \sin\theta = m \frac{1}{\Lambda} \lambda \qquad (28.7)$$

The total volume of the spectro-interferometer is thus 320 cm^3 (height 200 mm, width and length 40 mm), including the sample, the relay optics, and the detector. Note that once the flux is injected in the spectrometer (i.e., using a fibered V-groove), there is no moving part up to the detector; interference fringes and spectral dispersion are obtained directly on the detector. In order to reduce the footprint, a trade-off can be obtained by reducing the focal length and therefore the spectral resolution of the device.

We studied a waveguide grating consisting of 330 holes with a period of 30 μm, realized by femtosecond laser writing. In order to determine the resolution of the set-up, a scan between 1560 and 1587 nm was done.
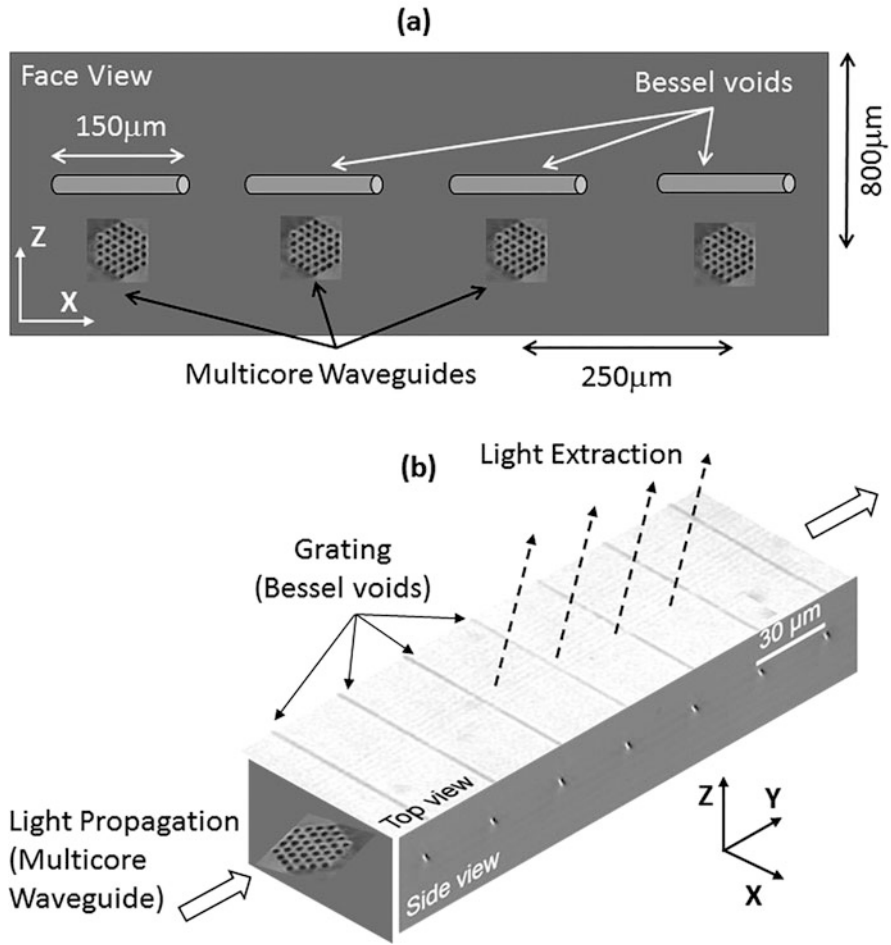
Fig. 28.24 (**a**) Face view of the whole structure showing four parallel multicore waveguides and their respective Bessel sampling centers above them. Typical dimensions are given in the figure. (**b**) 3D view of the device showing the disposition of the nanovoid array positioned transverse to the waveguide and the axis orientation. (Reproduced from Martin et al. [36])

As shown in the precedent figure, peak intensity moves on the detector as we scan the wavelength. The images on Fig. 28.27 show the short wavelength peak moving to the right as wavelength is increased. We can verify that a modification of 3 nm implies a peak shift of 30 pixels, that is, each pixel corresponds to 0.1 nm, which is the theoretical expected value.
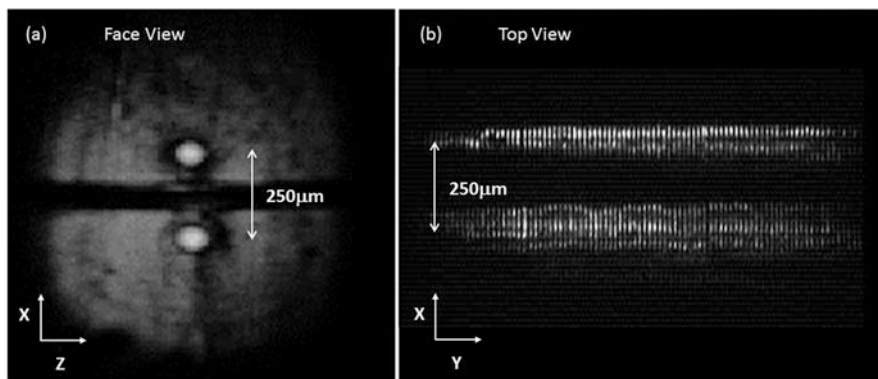
Fig. 28.25 Near IR observation of two parallel waveguides and the sampling centers when illuminated with a 1.56 μm laser. (**a**) Direct transmission on the FLIR camera, showing the two modes of two adjacent channel waveguides. (**b**) Top view as signal is extracted with the sampling centers and imaged on the Goodrich Camera using a simple microscope objective. (Reproduced from Martin et al. [36])
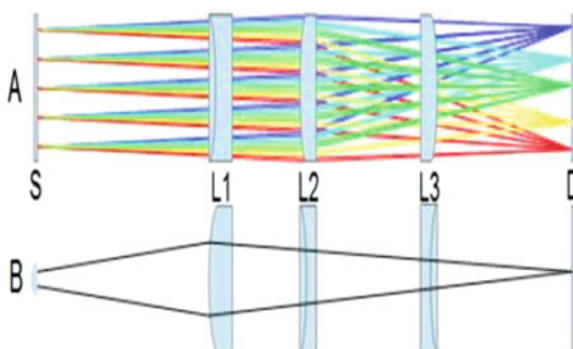

Fig. 28.26 Experimental set-up using a lens triplet, allowing for angular discrimination of the different wavelengths in the optical beam. (**a**) Sketch of optical rays along the vertical waveguide propagation axis. (**b**) Front view sketch, showing how the angular divergence of the signal extracted is focused on the detector. (From Martin et al. [36])

Using two parallel waveguides, one can then superimpose the signal to obtain a spectro-interferometer. The optical scheme is shown in Fig. 28.28.
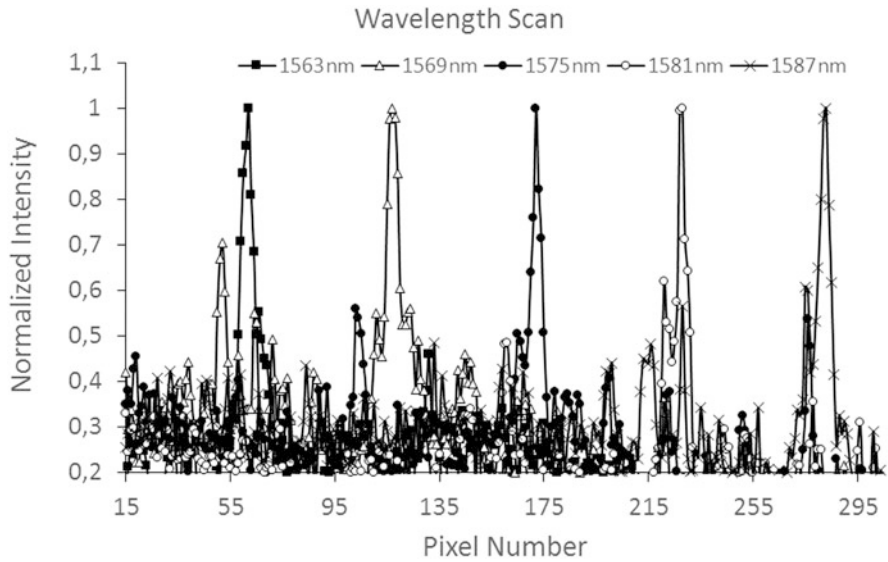
Fig. 28.27 Detected peak on an array of pixels, as the wavelength is scanned within the source tuning range. Side lobes are visible, due to inhomogeneous grating period fabrication, and induce crosstalk (see, e.g., the secondary lobe at 1569 nm (open triangles) close to the main peak at 1563 nm (filled squares)). (Reproduced from Martin et al. [36])
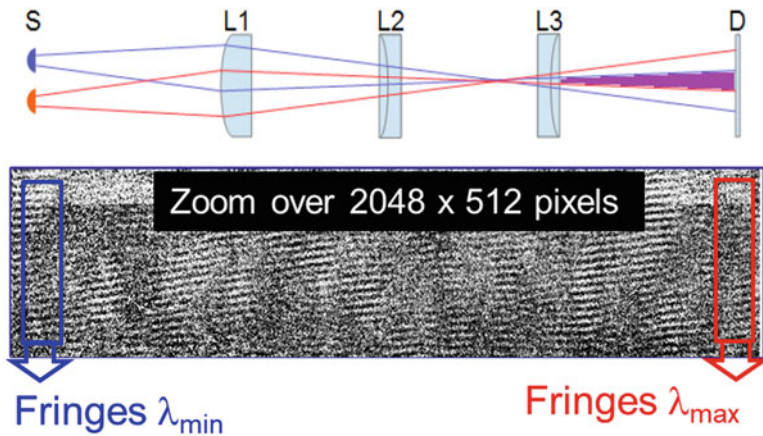

Fig. 28.28 (Top) Experimental set-up using a lens triplet, allowing for imaging two parallel waveguides on the detector and, by slightly defocusing, obtaining an overlap of the optical signals. (Bottom) Fringes obtained on the detector from the superposition of the two waveguides, with the wavelength increasing from left to right

6.3   Other Applications: Image Reconstruction, Pupil Remapping, and Wavelength Filtering (Bragg Filters)

The case of multiple beam recombination is being explored today for image reconstruction in ophthalmology or telecom transmission in order to correct wavefront errors as an alternative to complex adaptive optics systems [20]. Some flagship instruments using multiple sub-aperture recombination like FIRST/SUBARU [10] use this technique for image reconstruction and model fitting in astronomy using complex photonic chips (see Fig. 28.29 left). One can observe that increasing the number of channels to combine implies being rapidly limited by the length of the wafer (typically limited to 5 inches). Besides, two-dimensional (2D) waveguide routing introduces in-plane crossings that imply unwanted phase delays and crosstalk. Therefore, densification of optical functions by accessing the three-dimensional (3D) real space would be a very interesting solution if technologically feasible (see Fig. 28.29 right). Finally, if the full 3D IR photonic instrument is low-energy demanding and has a minimal footprint, avoiding any moving part and going from the collecting aperture to the integrated detector all monolithically, it would be of huge interest for applications in remote sensing: drone or nanosat applications (PICSAT [43]), in particular in the field of gas monitoring (SPOC [13]; NANOCARB [22]).

Some preliminary results on these types of systems are shown here (Fig. 28.30), with a 3D 3T beam interferometer made by DLW in a borosilicate glass [45].

By injecting light in channels 1 and 3 and using and external mirror for relative optical path modulation, we can scan the wideband fringes and, after Fourier transform, recover the spectrum of light. This preliminary results allow to validate the principle of sampling the 3D 3T. More details can be found in [35].
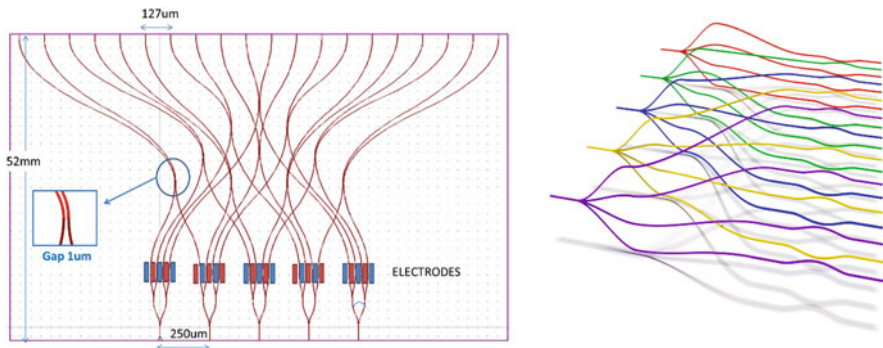

Fig. 28.29 (*Left*) Classical 2D concept of the 5T FIRST beam combiner, implying 20 parallel channel waveguides to be combined by pairs. Note the number of in-plane crossings. (*Right*) Concept of a laser-written 5T FIRST 3D solution, allowing to reduce propagation length and remove in-plane crossings and therefore increasing global transmission
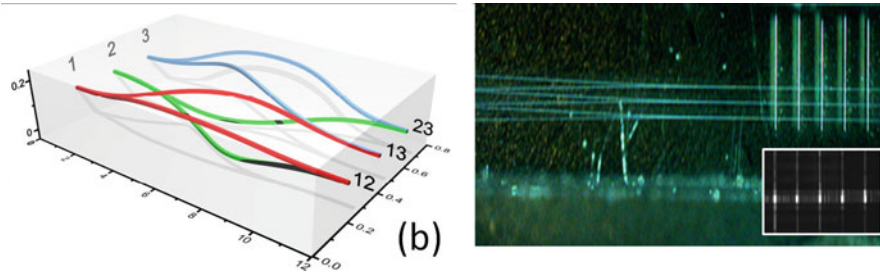
Fig. 28.30 (*Left*) Sketch of a 3D 3T beam combiner. (Reproduced from Rodenas et al. [45]). (*Right*) Image of the fabricated 3D 3T and the sampling centers using DLW. In the inset is shown the image of the radiating sampling centers when an IR laser is injected at the input
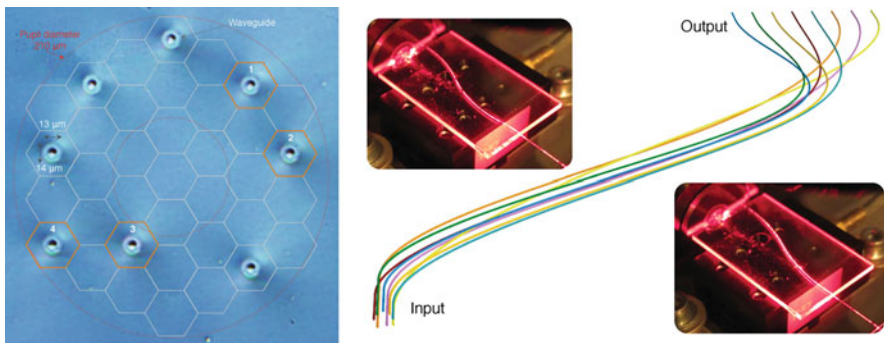

Fig. 28.31 (*Left*) Image of the nonredundant input, fabricated in the sample by DLW. (*Right*) Sketch and images of the optical beam redistribution from a 2D input to a linear 1D output. (Reproduced from Jovanovic et al. [27])

Pupil Remapping

One powerful interferometric technique is aperture masking [53] which offers precise calibration of wavefront structure for angular separations from the target star of around λ/D. This is achieved by recording Fizeau interferograms generated by a nonredundant sparse aperture mask placed in a reimaged telescope pupil plane. Such a scheme has been shown to be highly robust against the degrading effects of atmospheric phase noise, particularly when the self-calibrating closure phase observable [1] is utilized [30, 32].

An example of a pupil remapping system developed for astronomy, using direct laser writing, is Dragonfly [27], which optical waveguide redistribution is shown in Fig. 28.31.

Using DLW, the nonredundant pupil plane is redirected towards a line output that is later reimaged on the detector. The spectrum is obtained by classical prism dispersion in this case.

Waveguide Bragg Gratings (OH Suppression)

A waveguide Bragg grating (WBG) [7, 28, 38] is a type of distributed Bragg reflector constructed in a short segment of optical waveguide that reflects particular wavelengths of light and transmits all others. This is achieved by creating a periodic variation in the refractive index of the waveguide core, which generates a wavelength-specific dielectric mirror. Hence a WBG can be used as an inline optical waveguide to block certain wavelengths, or it can be used as wavelength-specific reflector.

DLW has been used to fabricate fully integrated photonic lanterns with incorporated WBG to provide spectral filtering and discuss potential astronomical applications [49]. Femtosecond laser-written WBG has been demonstrated using various techniques, such as single axial point-by-point [34] or a square-wave modulated pulse train [57]. In a typical example, DLW allows passing from an input photonic lantern to a planar distribution of single-mode waveguides, each with a specific Bragg grating period, and then restructuring an output photonic lantern, where the designed wavelengths will be rejected.

In this chapter we have shown the interest of DLW for its versatility and interest in the fabrication of 3D photonic systems, allowing for accurate fabrication of waveguides, nano-scattering centers, Bragg gratings, and complex interferometers. We have focused on a particular family of Fourier transform spectrometers (SWIFTS approach) and presented also some interesting applications in astronomy. There is no doubt that with the increasing performances of femtosecond laser writing, more complex systems allowing for multiple beam combination and on-chip spectrometry will be developed, paving the way for spectro-imaging at high pixel resolution.

References

1. J. Baldwin, C. Haniff, C. Mackay, et al., Closure phase in high-resolution optical imaging. Nature **320**, 595–597 (1986)
2. M.K. Bhuyan, F. Courvoisier, P.A. Lacourt, M. Jacquot, R. Salut, L. Furfaro, J.M. Dudley, High aspect ratio nanochannel machining using single shot femtosecond Bessel beams. Appl. Phys. Lett. **97**, 081102 (2010)
3. M. Bhuyan, P.K. Velpula, J.P. Colombier, T. Olivier, N. Faure, R. Stoian, Single shot high aspect ratio bulk nanostructuring of fused silica using chirp controlled ultrafast laser Bessel beams. Appl. Phys. Lett. **104**, 021107 (2014)
4. T.A. Birks, I. Gris-Sánchez, S. Yerolatsitis, S.G. Leon-Saval, R.R. Thomson, The photonic lantern. Adv. Opt. Photon. **7**, 107 (2015)
5. M. Bonduelle, G. Martin, I.H. Perez, A. Morand, C. d'Amico, R. Stoian, G. Zhang, G. Cheng, Laser written 3D 3T spectro-interferometer: study and optimisation of the laser-written nano-antenna, in *Proc. SPIE 11446, Optical and Infrared Interferometry and Imaging VII*, (13 December 2020), p. 114462T
6. M. Bonduelle, I. Heras, A. Morand, G. Ulliac, R. Salut, N. Courjal, G. Martin, Near IR stationary wave Fourier transform lambda meter in lithium niobate: Multiplexing and improving optical sampling using spatially shifted nanogroove antenna. Appl. Opt. **60**, D83–D92 (2021)

7. G. Brown, R.R. Thomson, A.K. Kar, N.D. Psaila, H.T. Bookey, Ultrafast laser inscription of Bragg-grating waveguides using the multiscan technique. Opt. Lett. **37**, 491 (2012)

8. F. Ceccarelli, S. Atzeni, A. Prencipe, R. Farinaro, R. Osellame, Thermal phase shifters for femtosecond laser written photonic integrated circuits. J. Light. Technol. **37**(17), 4275–4281 (2019)

9. G. Cheng, C. D'Amico, X. Liu, R. Stoian, Large mode area waveguides with polarization functions by volume ultrafast laser photoinscription of fused silica. Opt. Lett. **38**, 1924 (2013)

10. N. Cvetojevic, et al., FIRST, the pupil-remapping fiber interferometer at Subaru telescope: towards photonic beam-combination with phase control and on-sky commissioning results. Proc. SPIE 10701, Optical and Infrared Interferometry and Imaging VI, 107010A (10 July 2018)

11. K.M. Davis, K. Miura, N. Sugimoto, K. Hirao, Writing waveguides in glass with a femtosecond laser. Opt. Lett. **1024**(21), 1729–1731 (1996)

12. Y.N. Denisyuk, On the reproduction of the optical properties of an object by the wave field of its scattered radiation. Opt. Spectrosc. (USSR) **15**, 279–284 (1963)

13. T. Diard, F. de la Barrière, Y. Ferrec, N. Guérineau, S. Rommeluère, E. Le Coarer, G. Martin, Compact high-resolution micro-spectrometer on chip: spectral calibration and first spectrum, in *Proc. SPIE 9836, Micro- and Nanotechnology Sensors, Systems, and Applications VIII*, (25 May 2016), p. 98362W

14. G. Douglass, F. Dreisow, S. Gross, S. Nolte, M.J. Withford, Towards femtosecond laser written arrayed waveguide gratings. Opt. Express **23**(16), 21392–21402 (2015)

15. G. Douglass, F. Dreisow, S. Gross, M.J. Withford, Femtosecond laser written arrayed waveguide gratings with integrated photonic lanterns. Opt. Express **26**(2), 1497–1505 (2018)

16. G. Douglass, A. Arriola, I. Heras, G. Martin, E. Le Coarer, S. Gross, M.J. Withford, Novel concept for visible and near infrared spectro-interferometry: Laser-written layered arrayed waveguide gratings. Opt. Express **26**, 18470–18479 (2018)

17. C. Dragone, An N × N optical multiplexer using a planar arrangement of two star couplers. IEEE Photon. Technol. Lett. **3**(9), 812–815 (1991)

18. I.V. Dyakonov et al., Reconfigurable photonics on a glass chip. Phys. Rev. Appl. **10**(4), 044048 (2018)

19. F. Flamini et al., Thermally reconfigurable quantum photonic circuits at telecom wavelength by femtosecond laser micromachining. Light Sci. Appl. **4**, e354 (2015)

20. T. Fusco, et al. Optimization of a Shack-Hartmann-based wavefront sensor for XAO systems. Proc. SPIE 5490, Advancements in Adaptive Optics, (25 October 2004)

21. D. Gabor, A new microscopic principle. Nature **161**, 777–778 (1948)

22. S. Gousset, et al., NANOCARB-21: A miniature Fourier-transform spectro-imaging concept for a daily monitoring of greenhouse gas concentration on the Earth surface, in *International Conference on Space Optics—ICSO 2016*, vol. 10562, (International Society for Optics and Photonics, 2017). https://hal.archives-ouvertes.fr/hal-01401371

23. N.C. Harris et al., Efficient, compact and low loss thermo-optic phase shifter in silicon. Opt. Express **22**(9), 10487–10493 (2014)

24. R. He, I. Hernández-Palmero, C. Romero, J.R. Vázquez de Aldana, F. Chen, Three-dimensional dielectric crystalline waveguide beam splitters in mid-infrared band by direct femtosecond laser writing. Opt. Express **22**, 31293–31298 (2014)

25. J. Hu, C.R. Menyuk, Understanding leaky modes: Slab waveguide revisited. Adv. Opt. Photonics **1**, 58–106 (2009)

26. M. Hughes, W. Yang, D. Hewak, Fabrication and characterization of femtosecond laser written waveguides in chalcogenide glass. Appl. Phys. Lett. **90**, 131113 (2007)

27. N. Jovanovic et al., Starlight demonstration of the Dragonfly instrument: An integrated photonic pupil-remapping interferometer for high-contrast imaging. Mon. Not. R. Astron. Soc. **427**, 806–815 (2012)

28. S. Kroesen, W. Horn, J. Imbrock, C. Denz, Electro-optical tunable waveguide embedded multiscan Bragg gratings in lithium niobate by direct femtosecond laser writing. Opt. Express **22**(19), 23339–23348 (2014)

29. A. Labeyrie, J.P. Huignard, B. Loiseaux, Optical data storage in microfibers. Opt. Lett. **23**(4), 301–303 (1998)
30. S. Lacour, P. Tuthill, P. Amico, M. Ireland, D. Ehrenreich, N. Huelamo, A.-M. Lagrange, Sparse aperture masking at the VLT – I. Faint companion detection limits for the two debris disk stars HD 92945 and HD 141569. Astron. Astrophys. **532** (2011). https://doi.org/10.1051/0004-6361/201116712
31. E. le Coarer, S. Blaize, P. Benech, I. Stefanon, A. Morand, G. Lerondel, G. Leblond, P. Kern, J.M. Fedeli, P. Royer, Wavelength-scale stationary-wave integrated Fourier-transform spectrometry. Nat. Photonics **1**, 473 (2007)
32. J.P. Lloyd, F. Martinache, M.J. Ireland, et al., Direct Detection of the Brown Dwarf GJ 802B with Adaptive Optics Masking Interferometry, ApJL **650**, L131 (2006)
33. J. Loridat, S. Heidmann, F. Thomas, G. Ulliac, N. Courjal, A. Morand, G. Martin, All integrated lithium niobate standing wave Fourier transform electro-optic spectrometer. J. Lightwave Technol. **36**, 4900–4907 (2018)
34. G.D. Marshall, M. Ams, M.J. Withford, Direct laser written waveguide Bragg gratings in bulk fused silica. Opt. Lett. **31**, 2690 (2006)
35. G. Martin, J. R. Vázquez de Aldana, A. Rodenas, C. d'Amico, R. Stoian, Recent results on photonic devices made by laser writing: 3D 3T near IR waveguides, mid-IR spectrometers and electro-optic beam combiners, in *Proc. SPIE 9907, Optical and Infrared Interferometry and Imaging V*, (26 July 2016), p. 990739
36. G. Martin, M. Bhuyan, J. Troles, C. D'Amico, R. Stoian, E. Le Coarer, Near infrared spectro-interferometer using femtosecond laser written GLS embedded waveguides and nano-scatterers. Opt. Express **25**, 8386–8397 (2017)
37. J.C.F. Matthews et al., Manipulation of multiphoton entanglement in waveguide quantum circuits. Nat. Photonics **3**(6), 346–350 (2009)
38. B.W. McMillen, M. Li, S. Huang, B. Zhang, K.P. Chen, Ultrafast laser fabrication of Bragg waveguides in chalcogenide glass. Opt. Lett. **39**(12), 3579–3582 (2014)
39. B.J. Metcalf et al., Quantum teleportation on a photonic chip. Nat. Photonics **8**(10), 770–774 (2014)
40. S. Minardi, G. Cheng, C. D'Amico, R. Stoian, A low power threshold photonic saturable absorber in nonlinear chalcogenide glass. Opt. Lett. **40**, 257 (2015)
41. A. Morand, I. Heras, G. Ulliac, E. Le Coarer, P. Benech, N. Courjal, G. Martin, Improving the vertical radiation pattern issued from multiple nano-groove scattering centers acting as an antenna for future integrated optics Fourier transform spectrometers in the near IR. Opt. Lett. **44**, 542–545 (2019)
42. H.-D. Nguyen, A. Ródenas, J.R. Vázquez de Aldana, G. Martín, J. Martínez, M. Aguiló, M.C. Pujol, F. Díaz, Low-loss 3D-laser-written mid-infrared LiNbO3 depressed-index cladding waveguides for both TE and TM polarizations. Opt. Express **25**, 3722–3736 (2017)
43. M. Nowak et al., Reaching sub-milimag photometric precision on Beta Pictoris with a nanosat: The PicSat mission, in *Space Telescopes and Instrumentation 2016: Optical, Infrared, and Millimeter Wave*, vol. 9904, (International Society for Optics and Photonics, Bellingham, 2016)
44. G. Perrin, F. Malbet, J. Monnier, Astrophysics with closure phases. Eur. Astron. Soc. Publ. Ser. **6**, 213–213 (2003)
45. A. Rodenas, G. Martin, B. Arezki, N. Psaila, G. Jose, A. Jha, et al., Three-dimensional mid-infrared photonic circuits in chalcogenide glass. Opt. Lett. **37**(3), 392–394 (2012)
46. G. Sagnac, Sur la preuve de la réalité de l'éther lumineux par l'expérience de l'interférographe tournant. CRAS (Paris) **157**, 708–710, 1410–1413 (1913)
47. B. E. A. Saleh, M. C. Teich (eds.), *Fundamentals of Photonics, Chap. 18* (Wiley & Sons, New York, 1991)
48. M.K. Smit, C. Van Dam, PHASAR-based WDM-devices: Principles, design and applications. IEEE J. Sel. Top. Quantum Electron. **2**(2), 236–250 (1996)
49. I. Spaleniak, S. Gross, N. Jovanovic, et al., Multiband processing of multimode light: Combining 3D photonic lanterns with waveguide Bragg gratings. Laser Photonics Rev. **8**, L1–L5 (2014)

50. F. Thomas, S. Heidmann, M. de Mengin, N. Courjal, G. Ulliac, A. Morand, P. Benech, E. Le Coarer, G. Martin, First results in near and mid IR lithium niobate-based integrated optics interferometer based on SWIFTS-Lippmann concept. J. Lightwave Technol. **32**, 3736–3742 (2014)
51. F. Thomas, S. Heidmann, J. Loridat, M. de Mengin, A. Morand, P. Benech, C. Bonneville, T. Gonthiez, E. Le Coarer, G. Martin, Expanding sampling in a SWIFTS-Lippmann spectrometer using an electro-optic Mach-Zehnder modulator, in *Proc. SPIE 9516, Integrated Optics: Physics and Simulations II*, (1 May 2015), p. 95160B
52. R.R. Thomson, T.A. Birks, S.G. Leon-Saval, A.K. Kar, J. Bland-HawtHorn, Ultrafast laser inscription of an integrated photonic lantern. Opt. Express **19**, 5698–5705 (2011)
53. P.G. Tuthill, J.D. Monnier, W.C. Danchi, Aperture masking interferometry on the Keck I Telescope: New results from the diffraction limit, in *Proc. SPIE 4006, Interferometry in Optical Astronomy*, (5 July 2000)
54. P.K. Velpula, M. Bhuyan, F. Courvoisier, H. Zhang, J.P. Colombier, R. Stoian, Spatio-temporal dynamics in nondiffractive Bessel ultrafast laser nanoscale volume structuring. Laser Photonics Rev. **2**, 230 (2016)
55. M.M. Vogel, M. Abdou-Ahmed, A. Voss, T. Graf, Very-large-mode-area, single-mode multi-core fiber. Opt. Lett. **34**, 2876 (2009)
56. J. Wang et al., Experimental quantum Hamiltonian learning. Nat. Phys. **13**(6), 551–555 (2017)
57. H. Zhang, S.M. Eaton, P.R. Herman, Opt. Lett. **32**, 2559–2561 (2007)
58. A. Zoubir, C. Lopez, M. Richardson, K. Richardson, Femtosecond laser fabrication of tubular waveguides in poly(methyl methacrylate). Opt. Lett. **29**, 1840–1842 (2004)